Bulletin of Volcanology (2025) 87:98
https://doi.org/10.1007/s00445-025-01880-7

RESEARCH ARTICLE

Near-surface anomalies within Solfatara Volcano, Campi Flegrei, Italy, revealed using magnetic gradient measurements and 3D electrical resistivity data

Vincenzo Di Fiore[1] · Daniela Tarallo[1] · Giuseppe Cavuoto[1] · Michele Punzo[1] · Pier Paolo G. Bruno[2]

Received: 13 June 2025 / Accepted: 5 September 2025 / Published online: 9 October 2025
© The Author(s) 2025

Abstract
This paper presents a new high-resolution magnetic map of the Solfatara crater, derived from magnetic gradient measurements. Using the gradient of the magnetic tensor, rather than the gradient of the magnetic vector, enhances the spatial resolution of magnetic anomalies. This case study demonstrates the superior capability of magnetic tensor gradient measurements in accurately locating and interpreting near-surface anomalies compared to standard magnetic methods. The new magnetic map of the inner part of Solfatara reveals clear NE and NW trends that align with Apennine and anti-Apennine structural orientations. The total magnetic intensity field is characterized by numerous short-wavelength anomalies (10–20 m), which are associated with shallow petrophysical and structural heterogeneities near the crater surface. The significance of this high-resolution magnetic dataset lies in its potential to improve the understanding and interpretation of the shallow hydrothermal system and volcanic features of Solfatara, a key site of the recent unrest at Campi Flegrei. Finally, we present an example of the joint application of full magnetic gradient tensor measurements and 3D electrical resistivity data for anomaly characterization.

Keywords Magnetic map · Electrical resistivity tomography · Magnetic gradient tensor · Solfatara · Campi Flegrei

Introduction

The Campi Flegrei caldera is one of the most complex and active volcanic systems in the world, characterized by persistent hydrothermal activity, seismic swarms, ground deformation, and periodic degassing. Within this setting, the Solfatara crater represents a key site for studying shallow volcanic and hydrothermal processes. Geophysical investigations of Solfatara using seismic tomography, electrical resistivity imaging, and electromagnetic surveys (Amoroso et al. 2018; Byrdina et al. 2014; Bruno et al. 2007, 2017; Gresse et al. 2017; Siniscalchi et al. 2019; Troiano et al. 2019) have revealed a stratified subsurface structure influenced by fumarolic emissions, hydrothermal fluid pathways, and past eruptive events. One particularly significant feature is the Fangaia area, a low-lying zone within the crater where many of the most intense geothermal manifestations are located.

In this dynamic setting, magnetic methods can provide complementary insights into shallow structures and active hydrothermal processes. However, traditional magnetic surveys based on vector measurements are limited by their high sensitivity to orientation errors. For instance, even a small heading error of 0.1° can produce deviations of up to ~ 100 nT, severely compromising data accuracy (Beiki et al. 2012). In contrast, total magnetic intensity gradient ($\overrightarrow{\mathrm{TMIG}}$) measurements are far less susceptible to orientation inaccuracies. This is because magnetic gradients primarily reflect shallow, local sources, such as hydrothermal or volcanic features, rather than the deep, core-originated background magnetic field, which typically has an intensity of ~ 50,000 nT. Moreover, the natural geomagnetic gradient from the Earth's core is very small (about 0.01–0.03 nT/m), making gradient-based techniques particularly suitable for near-surface investigations.

A major advantage of gradient methods is the ability to reduce background noise caused by distant ionospheric and

Editorial responsibility: M. Edmonds.

✉ Daniela Tarallo
daniela.tarallo@cnr.it

[1] Institute of Heritage Science-CNR, Naples, Italy

[2] DiSTAR – Università "Federico II", Naples, Italy

magnetospheric currents, such as diurnal variations or geomagnetic storms, through "common mode rejection," i.e., the ability of gradient measurements to suppress common background signals (ionospheric, magnetospheric) while highlighting local anomalies (Clark 2013). Additionally, gradient surveys minimize the need for regional corrections often required in total magnetic intensity (TMI) datasets, since deeper crustal contributions (not relevant for near-surface exploration) are naturally suppressed (Zuo et al. 2017). Gradient approaches also mitigate electromagnetic interference, which can severely affect marine or volcanic geophysical surveys. For example, Di Fiore et al. (2019) reported external fields generating an electromotive force of 1184 mV, comparable in magnitude to the signal of interest, highlighting the importance of robust acquisition strategies.

The benefits of $\overrightarrow{\text{TMIG}}$ surveys have long been recognized. Hood (1965, 1981) and Hood and Teskey (1989) derived vertical gradients from TMI data, while Hardwick (1996, 1999) explored horizontal gradients. In marine environments, Harrison and Southam (1991) demonstrated the advantages of gradient mapping in reducing magnetic noise and orientation drift. Practically, $\overrightarrow{\text{TMIG}}$ surveys employing arrays of 2–4 sensors can approximate full vector gradients with less sensitivity to orientation errors. Although $\overrightarrow{\text{TMIG}}$ data do not provide the full level of detail available from magnetic gradient tensor (MGT) measurements, they retain many of the same advantages. Advanced processing techniques, such as Fourier-based analysis, can further extract vector and tensor information from high-quality TMI data (Luo et al. 2015), enhancing the interpretation of shallow subsurface features.

This paper presents the first high-resolution magnetic gradient map of the Solfatara crater, derived from $\overrightarrow{\text{TMIG}}$ measurements. Our study focuses on the northeastern sector of the crater, including the Fangaia area, where hydrothermal manifestations are most intense. By comparing magnetic gradient data with 3D resistivity imaging, we identified a magnetic anomaly coinciding with an electrically resistive body of approximately 165,000 m^3 ($80 \times 115 \times 18$ m). This volume, previously interpreted as a zone of intense hydrothermal alteration, is better resolved in the newly acquired magnetic gradient tensor maps, which provide additional constraints on its geometry and significance.

Overall, this study contributes to a better understanding of shallow volcanic structures and hydrothermal systems in Solfatara and, more broadly, the Campi Flegrei region. By introducing a high-resolution magnetic gradient map, something not previously available for this area, we open new opportunities for interpreting magnetic anomalies in terms of geological and hydrothermal processes. Furthermore, the rather joint application of $\overrightarrow{\text{TMIG}}$ measurements with 3D resistivity models demonstrates the strength of multidisciplinary geophysical approaches in resolving complex subsurface features. Beyond Solfatara, the methodologies applied here may serve as a model for future surveys in similarly challenging volcanic terrains worldwide, supporting hazard assessment and early warning strategies in densely populated and geologically active regions.

Geological settings

The Campi Flegrei volcanic field, located ~ 15 km west of Naples in the Campanian Plain (Italy), is among the most hazardous volcanic areas worldwide due to its explosive eruptive history and proximity to a densely populated region (Fig. 1).

Its origin is linked to two major caldera-forming supereruptions: the Campanian Ignimbrite (CI, ~ 39.8 ka; Giaccio et al. 2017) and the Neapolitan Yellow Tuff (NYT, ~ 15 ka; Deino et al. 2004). Subsequent subaerial and submarine activity has mostly occurred inside the caldera, generating numerous monogenic volcanoes. The last eruption took place at Monte Nuovo in 1538 A.D. Since the mid-twentieth century, Campi Flegrei has experienced three uplift crises (1950–1990) followed by subsidence. Renewed unrest started in (Isaia, et al., 2005), with accelerating seismicity, ground deformation, and gas compositional changes (Tramelli et al. 2023). Deformation shows a roughly circular pattern centered on Pozzuoli and tapering outward (Chiodini et al. 2001; 2007; 2016) and is mainly caused by heating and pressurization of the hydrothermal system rather than by shallow magma intrusion (Danesi et al. 2023; Chiodini et al. 2017). Seismicity concentrates in the Solfatara–Pisciarelli area, where hydrothermal activity and mud emissions are particularly intense (Esposito et al. 2023). Overall, the seismic activity in Campi Flegrei is a key factor in assessing volcanic risk and improving monitoring and mitigation strategies in this densely popular area (Orsi et al. 1999; De Siena et al. 2010; D'Auria et al. 2011; Di Luccio et al. 2015).

Geophysical investigations have progressively refined the understanding of the Campi Flegrei caldera structure. Large-scale geophysical analysis of airborne gravity and magnetic data collected by ENI over Campi Flegrei and the surrounding Campanian Plain was performed by Florio et al. (1999). Their study revealed a complex structural framework, with a major NE–SW lineament separating the magnetized Phlegraean region from a non-magnetic area to the east. Marine surveys focused on the submerged sector of the caldera in the Bay of Pozzuoli. Active-source seismic reflection data highlighted NE-trending faults, with additional NW structures inside the caldera (Finetti and Morelli 1974; Bruno et al. 2003; Bruno 2004; Judenherc and Zollo 2004). These studies suggested that caldera collapse in the marine sector is strongly controlled by NE–SW and NW–SE

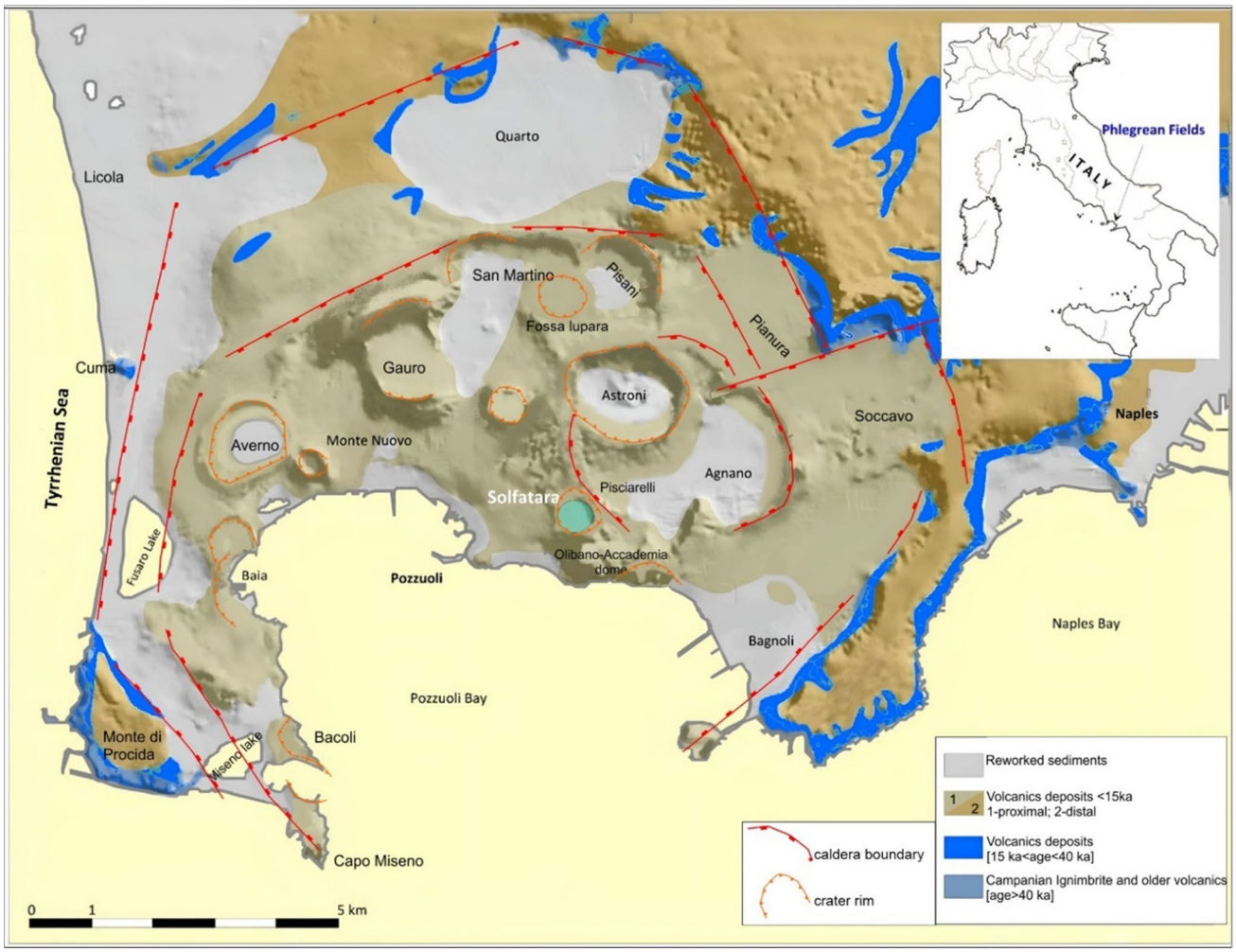

Fig. 1 Geological map of the Campi Flegrei caldera (modified from Troiano et al. 2019). The green circle marks the location of Solfatara crater, the study area discussed in this paper

tectonic discontinuities, with evidence of volcanic activity along fault planes.

Later, Vanorio et al. (2005) applied a multidisciplinary approach combining 3D P- and S-wave tomography with rock physics characterization. Their velocity models revealed a pronounced low-velocity anomaly down to 4 km depth—1.7–3.8 km/s for P-waves and 1.0–2.5 km/s for S-waves—interpreted as fractured, overpressured, gas- and fluid-saturated formations. Zollo et al. (2008) used active-source seismic reflection data from the Serapis experiment to image the deeper structure of the caldera, identifying high-amplitude reflections from the top of a widespread supercritical fluid-bearing rock formation at ~ 2700 m depth and a thick low-velocity layer at 7500 m depth interpreted as a mid-crustal partial melt zone beneath the caldera.

Recent seismic tomography studies using P- and S-waves have significantly refined our understanding of the Campi Flegrei caldera, highlighting its complex hydrothermal system and active fault network. High-resolution imaging has revealed fluid-rich zones beneath Pozzuoli and Solfatara, with elevated Vp/Vs ratios indicating possible pathways for gas and fluid migration closely linked to uplift and seismicity (Calò and Tramelli 2018; 2025). These works have also constrained the presence of a caprock at ~ 2 km depth, controlling fluid circulation and unrest dynamics. Relocation of seismic swarms (2000–2024) has shown that earthquakes cluster mainly beneath Solfatara/Pisciarelli within a fractured, fluid-saturated volume, while high-precision tomography has mapped active faults potentially capable of hosting moderate-magnitude events (Tramelli et al. 2021, 2022; Giudicepietro et al. 2021; Di Uccio et al. 2024).

Within this context, Solfatara volcano, located ~ 2 km east of Pozzuoli, represents the most active sector of the caldera. The crater shows intense fumarolic and hydrothermal activity both inside and along its flanks. Diffuse degassing occurs preferentially along faults and fractures acting as permeable

pathways for magmatic–hydrothermal fluids (De Martino et al. 2020). These structures developed during the most recent eruptive phase of Campi Flegrei (~4.2 ka; Isaia et al. 2009; Smith et al. 2011). Geological mapping (Isaia et al. 2015; Fig. 2) interprets Solfatara as a maar-diatreme structure, with ring faults and collapse features controlled by explosions, regional tectonics, and gravitational instability.

Shallow seismic reflection profiles support this interpretation (Bruno et al. 2017, Bernardinetti, and Bruno, 2019). Several volcanic units are associated with this structure, including the Agnano-Monte Spina tephra (4.5 ka), the Santa Maria delle Grazie scoria cone and ash (4.4 ka), the Monte Olibano and Accademia lava domes, the Olibano phreatic breccia, the Solfatara cryptodome, and tephra from Solfatara and Averno (4.2 ka).

The hydrothermal system of Solfatara releases several kilotons of fluids daily through diffuse soil emissions and fumaroles, with CO_2 fluxes estimated at 2000–3000 t/day (Cardellini et al. 2017). Gas composition and the extension of degassing areas have evolved over time, suggesting that magma degassing has reached a critical pressure, enhancing fluid input to the hydrothermal system (Chiodini et al. 2016; Cardellini et al. 2017). Soil CO_2 flux is spatially correlated with deformation and fault systems, indicating feedback between degassing and ground deformtion (De Martino et al. 2021).

Geoelectrical studies highlight the complexity of the shallow subsurface. A conductive layer beneath a shallow resistive vadose zone was imaged in the crater center (Bruno et al. 2007). Further surveys (Byrdina et al. 2014; Gresse et al. 2017) identified resistive bodies at 30–100 m depth, interpreted as gas-dominated reservoirs feeding fumaroles. Interpolated profiles suggest a ~60 m deep reservoir connected to the Bocca Grande fumarole by a narrow conduct (Gresse et al. 2017). Despite these results, information on the very shallow subsurface remains limited, justifying the use of high-resolution methods such as magnetic gradient measurements to better resolve near-surface structures and hydrothermal features.

Magnetic data

Magnetic data were collected entirely within the Solfatara crater, covering an area of approximately 40,000 m^2 (black segments in Fig. 2B). The survey employed gradient technique using a G858 Geometrics cesium vapor magnetometer/gradiometer. Each sensor contains a vapor cell where the resonance frequency of cesium atoms, in the presence of a magnetic field, is measured and used to infer field intensity. The instrument records the field with two independent sensors, and the difference between their readings, divided by the vertical or horizontal separation, yields the corresponding magnetic gradient.

The survey was carried out on foot, with sensors mounted 1 m apart both vertically and horizontally, the lower positioned 0.40 m above ground. They were fixed on a staff supported by a shoulder strap and connected to a console with an integrated GPS antenna receiving real-time differential corrections. The console, worn at the waist, allowed grid design and continuous monitoring of data acquisition. The "simple survey" mode was adopted, with a sampling rate of 10 Hz and a spatial sampling of 0.5 points per m^2. Both TMI and $\overrightarrow{\text{TMIG}}$ values were acquired for the horizontal and vertical directions.

Processing began with the removal of spurious disturbances (e.g., spikes) and proceeded to generate regular grids. Contributions from undesired sources were minimized through nonlinear de-spiking, detrending (to exclude deep contributions), and micro-leveling (to correct line-related artifacts). Kriging interpolation was applied to produce consistent magnetic grids. To avoid artifacts from non-periodicity or truncation, such as Gibbs oscillations, multiple grids with different resolutions and search radii were tested, and the versions with the most favorable spectral characteristics were selected.

Figure 3 The resulting TMI map of Solfatara. The high-resolution dataset reveals high TMI values (46,200–46,500 nT) in the central crater, decreasing toward the margins (~45,000 nT), with intermediate values (~46,000 nT) in the "Fangaia" area

In addition to TMI, we measured $\overrightarrow{TMIG}$ in the north, east, and vertical directions using a triaxial gradiometer system. The survey comprised 130 profiles, mainly NNW oriented, with some ENE cross-lines to provide control points (Fig. 2B). The same gridding and filtering procedures adopted for TMI were applied to$(\overrightarrow{FVMG})$, a common practice in potential field studies where horizontal and vertical derivatives serve as input for filters such as sunshading, analytic signal, tilt angles, and others (Cooper and Cowan 2011).

Figures 4 and 5 display the vertical and horizontal gradients derived from TMI. These maps emphasize linear features and zones of high gradient intensity, likely associated with the boundaries of magnetized bodies. Maximum values reach ~35 nT/m for the vertical gradient ($\overrightarrow{\text{FVMG}}$) and ~28 nT/m for the full horizontal gradient ($\overrightarrow{\text{FHMG}}$). Some structures also exhibit NE–SW trends, consistent with larger-scale features observed in the aeromagnetic survey of Florio et al. (1999).

Within the TMI map (Fig. 3), we identified a localized high-intensity, ellipsoidal anomaly in the northeastern sector of Solfatara (labeled "A" in Figs. 3, 4, and 5). To investigate its electrical properties, a 3D resistivity survey was carried out in this area, discussed in the following section. For

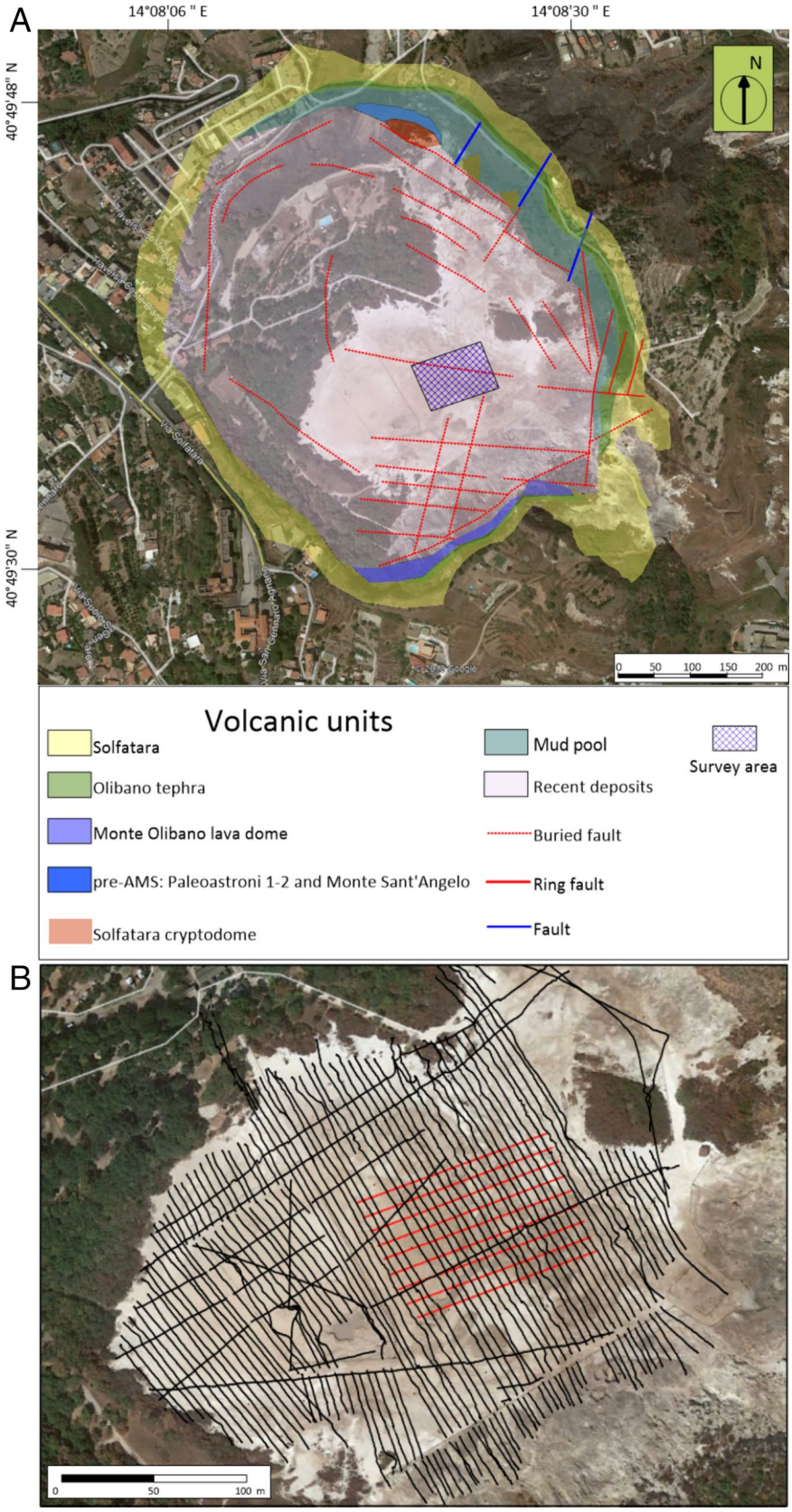

Fig. 2 **A** Geological map of Solfatara Volcano (modified from Isaia et al. (2015). **B** Image map (© 2022 Google) of Solfatara with survey layouts: the red line indicates the 3D electrical resistivity tomography (ERT) grid, while black lines indicate magnetic gradiometry profiles. These maps highlight the structural framework and the positioning of the geophysical surveys

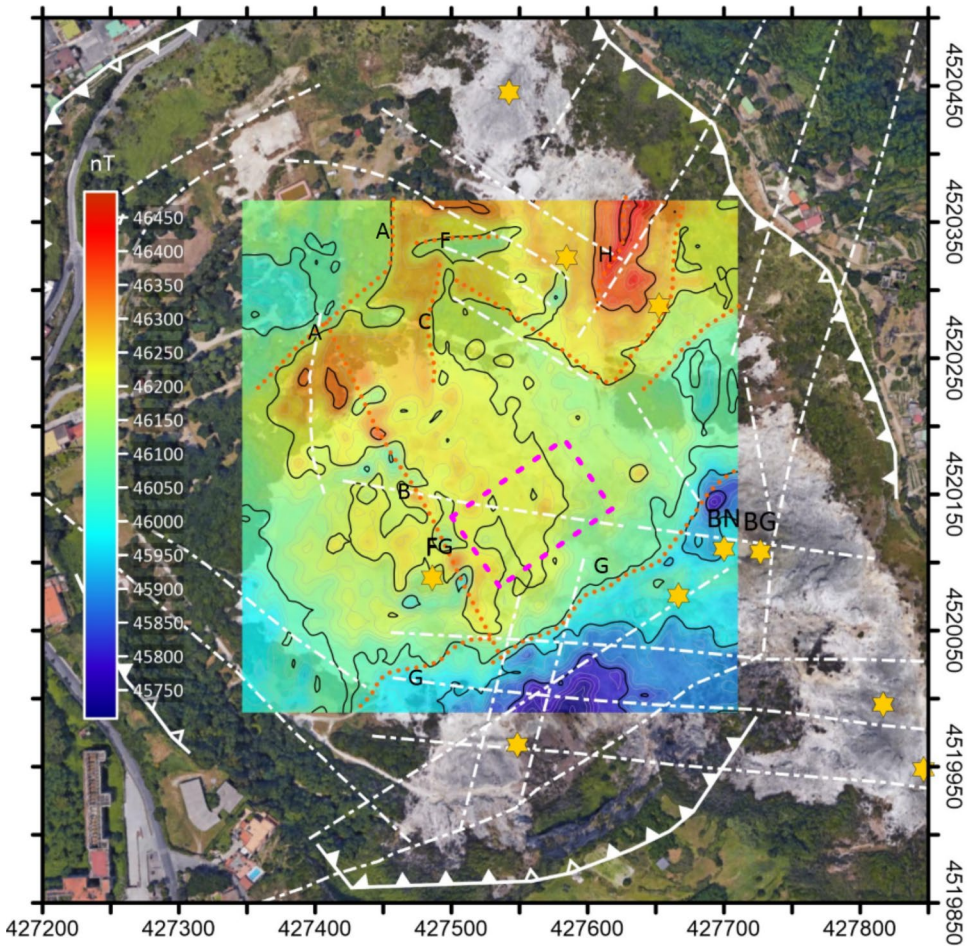

Fig. 3 Total magnetic intensity (TMI) map of Solfatara crater superimposed on image map (© 2022 Google). The outlined box marks the 3D ERT survey area. White dashed lines indicate fault orientations from Isaia et al. (2015), yellow stars mark eruptive centers, and red dotted lines emphasize linear features in the magnetic data interpreted as geological boundaries. TMI values range from ~ 45,000 to 46,500 nT

better interpretation of anomaly "A," both resistivity data and magnetic gradient tensor (MGT) components were used (see next sections). Since MGT analysis requires regularly gridded data, a "smooth and coherent" grid of tensor components was produced using the minimum curvature algorithm (Briggs 1974). Each tensor component was processed independently to avoid signal corruption. Although this approach does not preserve the Laplacian condition that defines tensors derived from scalar potential fields (Pedersen and Rasmussen 1990), it is recommended in areas with strong field curvature, such as near magnetic sources. To better understand how $\overrightarrow{\text{TMIG}}$ data acquired in fields were transformed into the MGT an illustrative flow chart is reported in Fig. 6.

Essentially, once the gradiometric magnetic data are acquired in the field, preliminary processing is carried out, including filtering (box 2), microleveling (box 3), and interpolation (box 4) to remove no-data points. Subsequently, after verifying the quasi-static field $\overrightarrow{B}$ conditions, integral transformations are applied (box 6) to derive the MGT.

A more comprehensive discussion is provided in Appendix "A." In these contexts, tensor interpolation methods that preserve physical properties are essential (Fitzgerald et al. 2010). The MGT data were then leveled using amplitude and phase information, with a heading correction analogous to scalar data adjustment (Neukirch et al. 2019), ensuring that the tensor averages retained their intrinsic physical properties.

Figures 7b–d show the triaxial gradient components of the TMI presented in Fig. 7a, in the UTM WGS84 zone 33 N coordinate system. Maximum values are ~ 30 nT/m in the downward (Z) direction, ~ 15 nT/m in the east (X) direction, and ~ 20 nT/m in the north (Y) direction. Regardless of coordinate transformation, the MGT can be expressed in terms of three invariants (I_0, I_1, and I_3; Pedersen and Rasmussen 1990). Figures 7e–f presents the I_1 and I_3 maps, which closely resemble the TMI distribution (Fig. 3) and highlight magnetic source boundaries. Notably, anomaly "A" appears more prominent in the I_1 map, underscoring its geophysical significance.

Electical resistivity data

The 3D resistivity survey was conducted in the area highlighted in Fig. 3, using a rectangular grid of 9 profiles. Each profile consisted of 24 electrodes spaced 5 m apart,

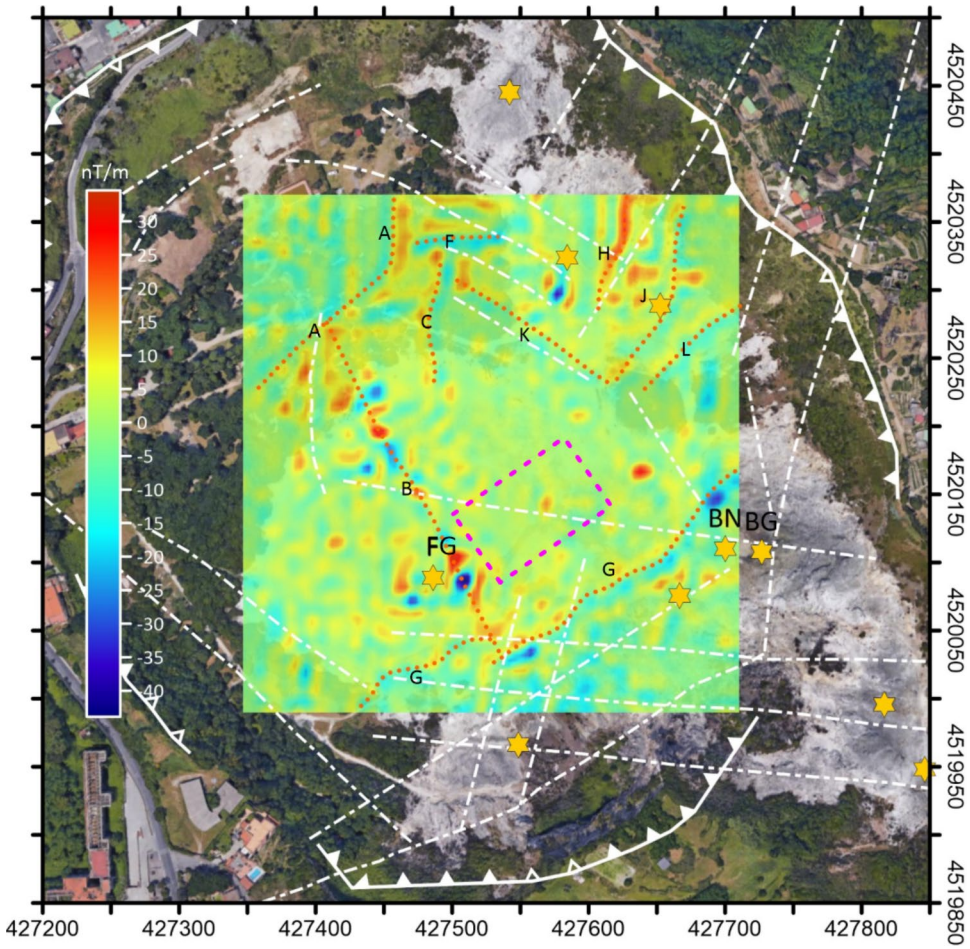

Fig. 4 Full vertical magnetic gradient (FVMG) map superimposed on an image map (© 2022 Google) of Solfatara Volcano. Symbols are the same as in Fig. 3. Gradient maxima (~35 nT/m) highlight linear features, likely corresponding to the edges of magnetized structures, some of which follow NE–SW trends consistent with regional tectonics

with 10 m spacing between adjacent profiles, for a total of 216 electrodes (Fig. 2B).

Given the relatively small coverage, we adopted a Wenner–Schlumberger array combined with a cross-diagonal survey. This acquisition strategy allowed fast and effective measurements of the electric potential along the profiles (*x*-axis), across the profiles (*y*-axis), and along 45° diagonal lines (Fig. 8).

The adopted methodology produced a high-quality 3D apparent resistivity dataset. As part of the processing workflow, preliminary 2D resistivity models were first evaluated to guide the construction of the 3D model. Initially, we generate an ensemble of resistivity models that represent potential solutions to the 2D ERT inverse problem. This ensemble is then refined by applying a statistical analysis to the associated residual distributions. Before proceeding with further analysis, we interpolate all models onto a unified mesh to enable consistent pixel-wise comparisons and calculations (Arboleda-Zapata et al. 2022).

The inversion was performed using a smoothness-constrained least-squares algorithm based on the "Occam's inversion" approach (Constable et al. 1987; LaBrecque et al. 1996), which iteratively generates the smoothest model that still fits the data within a chi-squared misfit threshold.

The final 3D resistivity model of the subsurface was obtained through an iterative inversion procedure. Prior to inversion, a rigorous data pre-processing and filtering workflow was applied to remove noise and anomalous values (Balasco et al. 2022). This included eliminating spurious spikes attributed to external noise or technical issues, correcting long-period signal drift, and quantifying signal amplitude to ensure data quality. The inversion relied on forward modelling combined with iterative optimization: at each step, the electric potential distribution was computed with the finite element method (FEM) within a fully 3D discretized Earth model, allowing simulation of the expected surface responses. The calculated and observed data were then compared, and the resistivity distribution was iteratively updated to minimize the misfit. Iterations proceeded until the residuals met a predefined convergence criterion, yielding the final 3D model. Figure 9 shows the distribution of apparent resistivity as a function of depth.

The final dataset included 12,471 quadrupoles (distributed as shown in Fig. 8). Table 1 reports inversion parameters, including the number of iterations and RMS misfit values

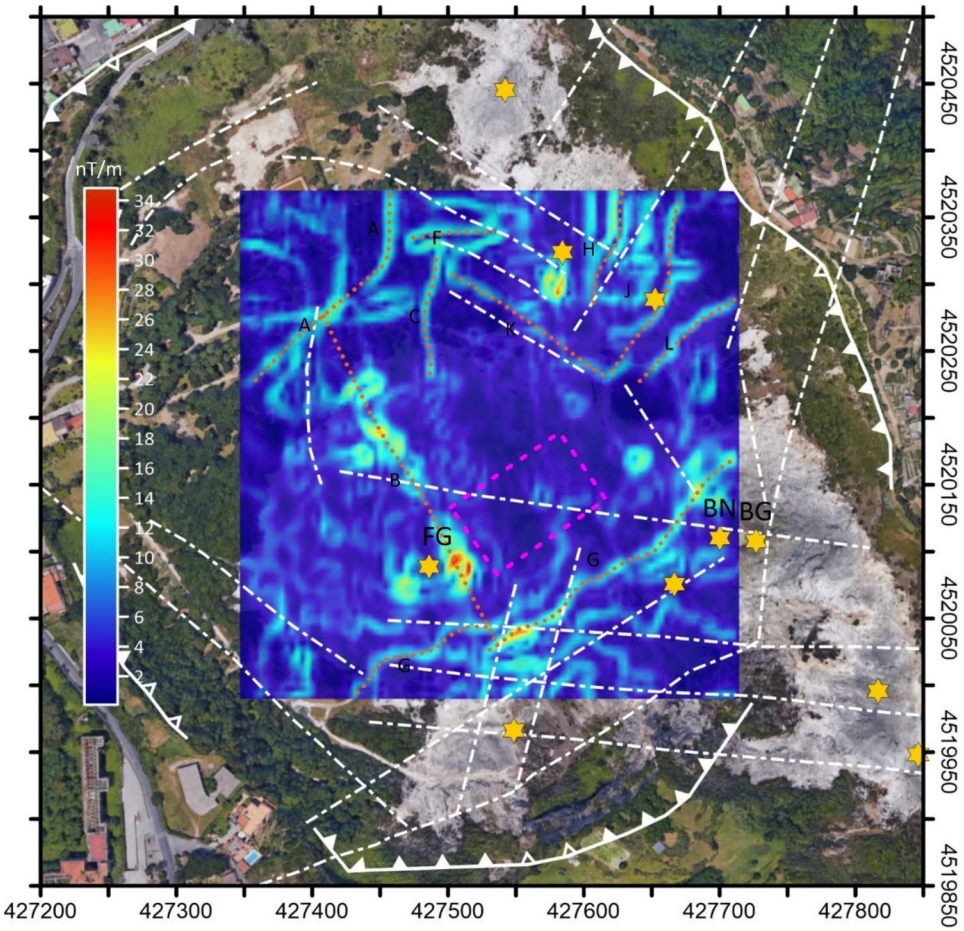

Fig. 5 Full horizontal magnetic gradient ($\overrightarrow{FHMG}$) map superimposed on an on an image map (© 2022 Google) of Solfatara Volcano. Symbols are the same as in Fig. 3. Gradient maxima (~28 nT/m) delineate linear boundaries of magnetized bodies. Together with Fig. 4, these data emphasize structural trends and the extent of anomaly "A" in the northeastern sector

(LaBrecque et al. 1999). On average, eight forward calculations were performed per iteration, and the RMS stabilized after the eighth iteration. The final RMS error was 2.05%, a highly satisfactory result considering the logistical challenges and the strong resistivity heterogeneity within the crater.

The 3D inversion was carried out using a finite-element forward solver coupled with a conjugate-gradient inversion routine. This implementation of Occam's inversion typically converges within 7–15 iterations, requiring only a single forward computation per iteration and avoiding the need to solve large systems of equations directly (deGroot-Hedlin and Constable 1990; LaBrecque et al. 1999).

The electrode interval has very high spatial resolution ($\Delta x = 2.5$ m, $\Delta y = 2.5$ m, $\Delta z = 1.25$ m) and resolves the subsurface down to ~23 m depth (Fig. 10).

We calculated the model resolution matrix by Day-Lewis et al. (2004). The model resolution values of the model blocks are given by the diagonal elements of this matrix.

The model is given by:

$$R = (J^T J + \lambda F)^{-1} \bullet \left(J^T J\right);$$

where J is the Jacobian matrix, λ is the weight that determines the trade-off between data misfit and regularization, and F is the model-weighting regularization matrix.

The model resolution matrix R can be interpreted as a filter through which the inversion method attempts to reconstruct the subsurface resistivity distribution. In the ideal case of perfect resolution, the elements along the main diagonal (Rjj) are equal to 1, while all off-diagonal elements are zero. In practice, however, the resolution values for most model blocks are significantly less than 1.0. These values indicate how well each model cell is resolved by the available data. It is important to note that the time required to compute the model resolution matrix increases proportionally to the cube of the number of model cells. Figure 10 shows the results of the resolution analysis of the ERT survey at the same depths as the electrical resistivity model obtained from the inversion. It is important to note that in the depth range between 7.10 and 12.10 m, where the resistivity anomaly is located, the resolution value R is approximately 0.80, indicating a good resolution of the model.

Figure 11 displays horizontal slices extracted from the 3D model, spanning depths between 4.60 m and 17.10 m below the surface, with a vertical interval of 2.5 m. The

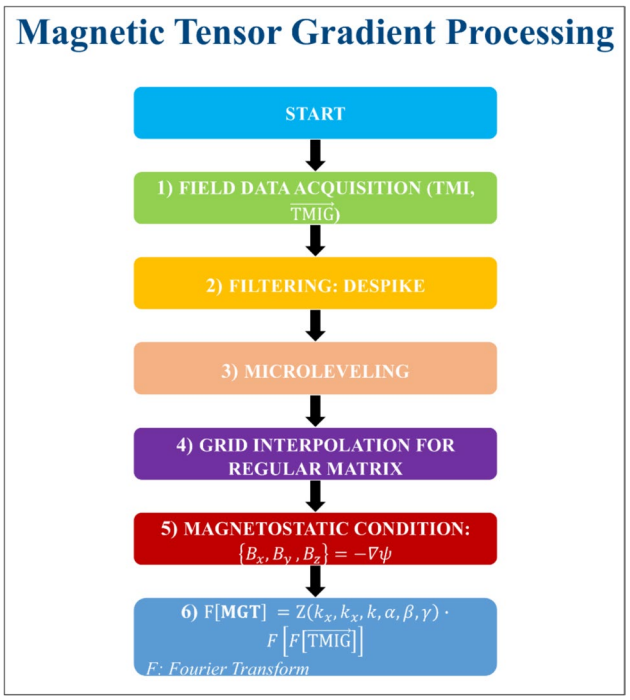

Fig. 6 Flowchart outlining the processing steps to derive the magnetic tensor gradient from the gradiometric magnetic data acquired in the field

investigated volume is generally characterized by low resistivity values, ranging between 3 and 35 Ωm. Several anomalies appear to align parallel or orthogonal to the survey profiles; these are most likely acquisition artifacts or geometrical footprints and were therefore disregarded in the interpretation. A distinct high-resistivity anomaly is observed at a depth of 9.60 m, with resistivity values of 25–30 Ωm, significantly higher than the surrounding material. This body is enclosed within a NE-elongated elliptical structure, approximately 10 m along its major axis and 5 m along its minor axis, which highlights its position across the slices shown in Fig. 5. This anomaly remains clearly detectable between depths of 7.10 and 14.60 m.

Importantly, this resistive body corresponds to features (i.e., anomaly A) observed both in the TMI map and in the magnetic gradient tensor invariant maps I1 and I3, confirming its geophysical significance (Fig. 7).

Results and discussion

The new total magnetic intensity (TMI) map, together with its horizontal and vertical gradients, provides key insights into the presence of previously unrecognized lineaments. According to Isaia et al. (2015) and Siniscalchi et al. (2019), the study area hosts faults trending NW–SE, SW–NE, and N–S, indicated as dashed white lines in Fig. 3. The TMI map and its derivatives (Figs. 3, 4, and 5) highlight additional linear magnetic features, shown as dotted red lines, which likely represent geological boundaries. These lineaments, predominantly located in the northern sector, may correspond to ring faults related to caldera collapse.

Several magnetic features, such as those labeled "J," "H," and "K" (Figs. 3, 4, and 5), align with fault orientations already reported by Isaia et al. (2015), while others are newly identified in this study. Notably, many faults previously mapped in the southern part of the area do not display a clear magnetic signature in our dataset.

Among the newly recognized structures, a NW–SE trending magnetic feature near the map center (labelled "B" in Figs. 3, 4, and 5) is of particular interest. This lineament, buried beneath recent Solfatara volcanic deposits, may represent a reactivated fault linked to the collapse of the Solfatara center. Siniscalchi et al. (2019) described a very shallow conductive zone beneath the Solfatara–Pisciarelli area, likely related to fault-controlled clay caps overlying an active hydrothermal zone. Lineament "B" intersects the eruptive center "FG" and terminates perpendicularly against another potential fault ("G"), oriented NE–SW, which separates low magnetic intensity zones in the southeast (< 46,000 nT ηT, blue contours) from higher magnetic values in the northwest (> 46,200 nT ηT, green/yellow contours).

Within the dashed rectangle in Fig. 3, we compared high-resolution electrical resistivity data (Fig. 11) with magnetic data and their derivatives. In this area, the TMI field ranges from 45,840 to 46,320 nT (Fig. 7a). The 3D resistivity model generally shows low values, but clear NE- and NW-trending resistive patterns emerge, including an ellipsoidal anomaly with horizontal dimensions of ~ 10 × 5 m and ~ 5 m thickness, located at depths between 7.1 and 12.1 m (Fig. 11).

Previous studies (Isaia et al. 2015; Gresse et al. 2017) interpreted this anomaly as a zone of intense hydrothermal activity. The largest resistivity contrast occurs at ~ 9 m depth, where the anomaly reaches ~ 30 Ωm against a ~ 5 Ωm background. Additional anomalies with resistivities around 15 Ωm also occur at similar depths, but their lack of magnetic correlation suggests they may represent acquisition artifacts (Fig. 3).

Magnetic gradient values vary strongly across the three directions (x, y, z) in correspondence with the resistivity anomaly. The vertical gradient reaches 35 nT/m, while the X- and Y-gradients are 10 nT/m and 18 nT/m, respectively (Figs. 7b–d). To refine source localization, we analyzed the invariant components of the magnetic gradient tensor (I_1 and I_3; Figs. 7e–f), following Bulent (2010). Invariant I_1 provides sharper resolution than the TMI, which suffers from higher noise levels, and both invariants (I_1 and I_3) highlight the anomaly more effectively than conventional gradient maps, reducing interpretive ambiguity.

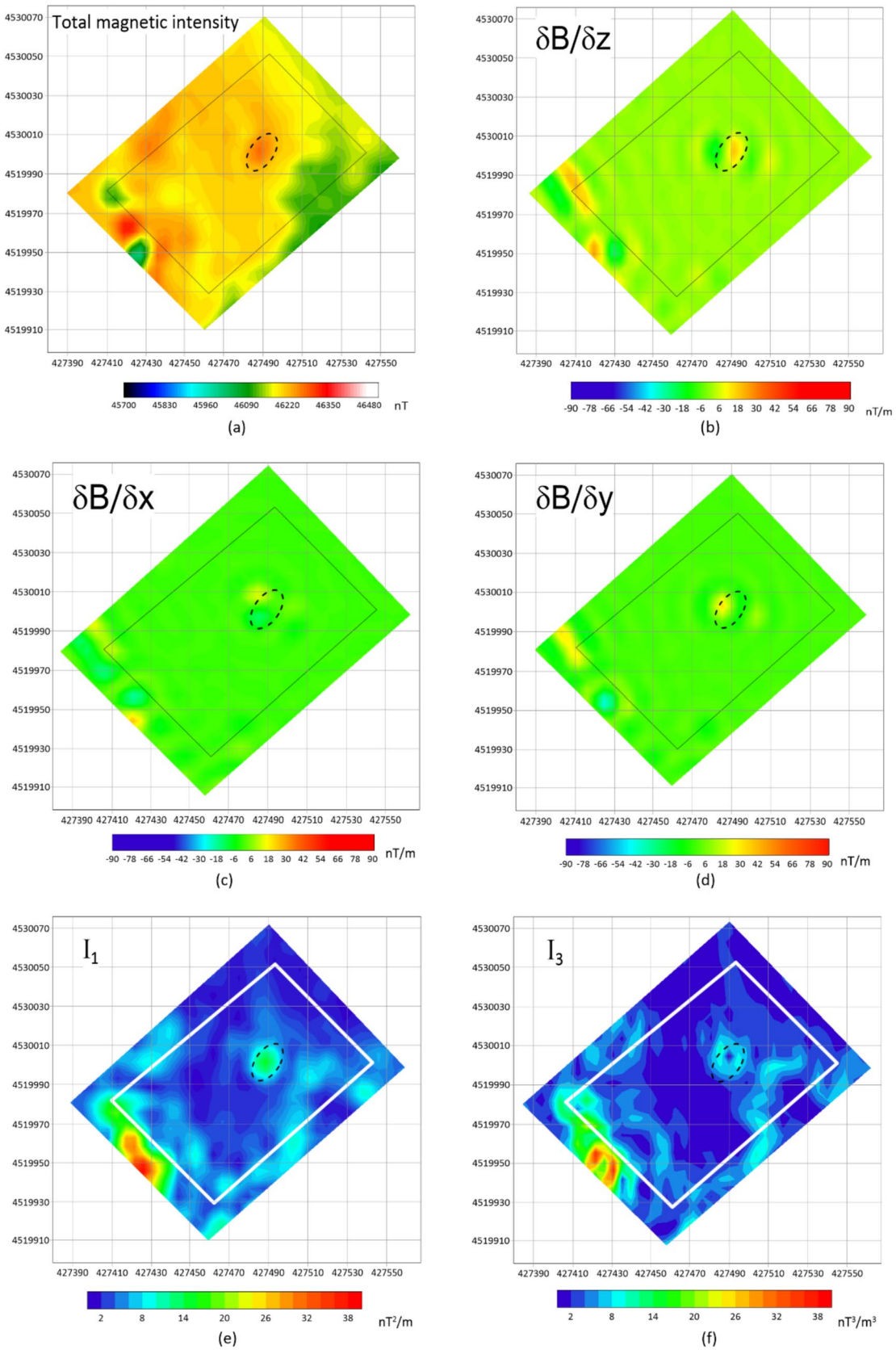
Total magnetic intensity
4530070
4530050
4530030
4530010
4519990
4519970
4519950
4519930
4519910
427390 427410 427430 427450 427470 427490 427510 427530 427550
45700 45830 45960 46090 46220 46350 46480 nT
(a)
δB/δz
-90 -78 -66 -54 -42 -30 -18 -6 6 18 30 42 54 66 78 90 nT/m
(b)
δB/δx
-90 -78 -66 -54 -42 -30 -18 -6 6 18 30 42 54 66 78 90 nT/m
(c)
δB/δy
-90 -78 -66 -54 -42 -30 -18 -6 6 18 30 42 54 66 78 90 nT/m
(d)
I1
2 8 14 20 26 32 38 nT²/m
(e)
I3
2 8 14 20 26 32 38 nT³/m³
(f)

◂**Fig. 7** Magnetic properties of the northeastern sector of Solfatara. **a** TMI map. **b–d** triaxial magnetic gradients along the Z, X, and Y directions (maximum values, 30, 15, and 20 nT/m, respectively). **e–f** invariant maps I1 and I3 derived from the magnetic gradient tensor (MGT). The white boxes indicate the 3D ERT survey area; while the dashed ellipse denotes the likely extent of influence from the resistive body. Data are in UTM WGS84 zone 33 N coordinates

Our interpretation of the 3D resistivity model draws on previous works (Isaia et al. 2015; Gresse et al. 2017; Byrdina et al. 2014). At 9.6 m depth, the resistive anomaly stands out with values of 25–30 Ωm compared to a 3–10 Ωm background, likely related to clay alteration within the hydrothermal system. Amoroso et al. (2018) developed a 3D S-wave velocity model of the Fangaia area, revealing low-velocity anomalies caused by water saturation and localized zones with Vs > 600 m/s between 10 and 15 m depth.

Our dataset reveals an additional property: the magnetic field gradients indicate anisotropy, with values of 35, 10, and 8 nT/m in the Z, X, and Y directions, respectively.

Unlike earlier studies, which relied solely on resistivity, our integrated dataset identifies a coincident magnetic anomaly. This dual evidence suggests an alternative interpretation: the anomaly may represent a large lithic ballistic block or an altered allochthonous block-possibly related to the Solfatara cryptodome, which crops out in the northeastern sector of the volcano. The magnetic anisotropy makes a

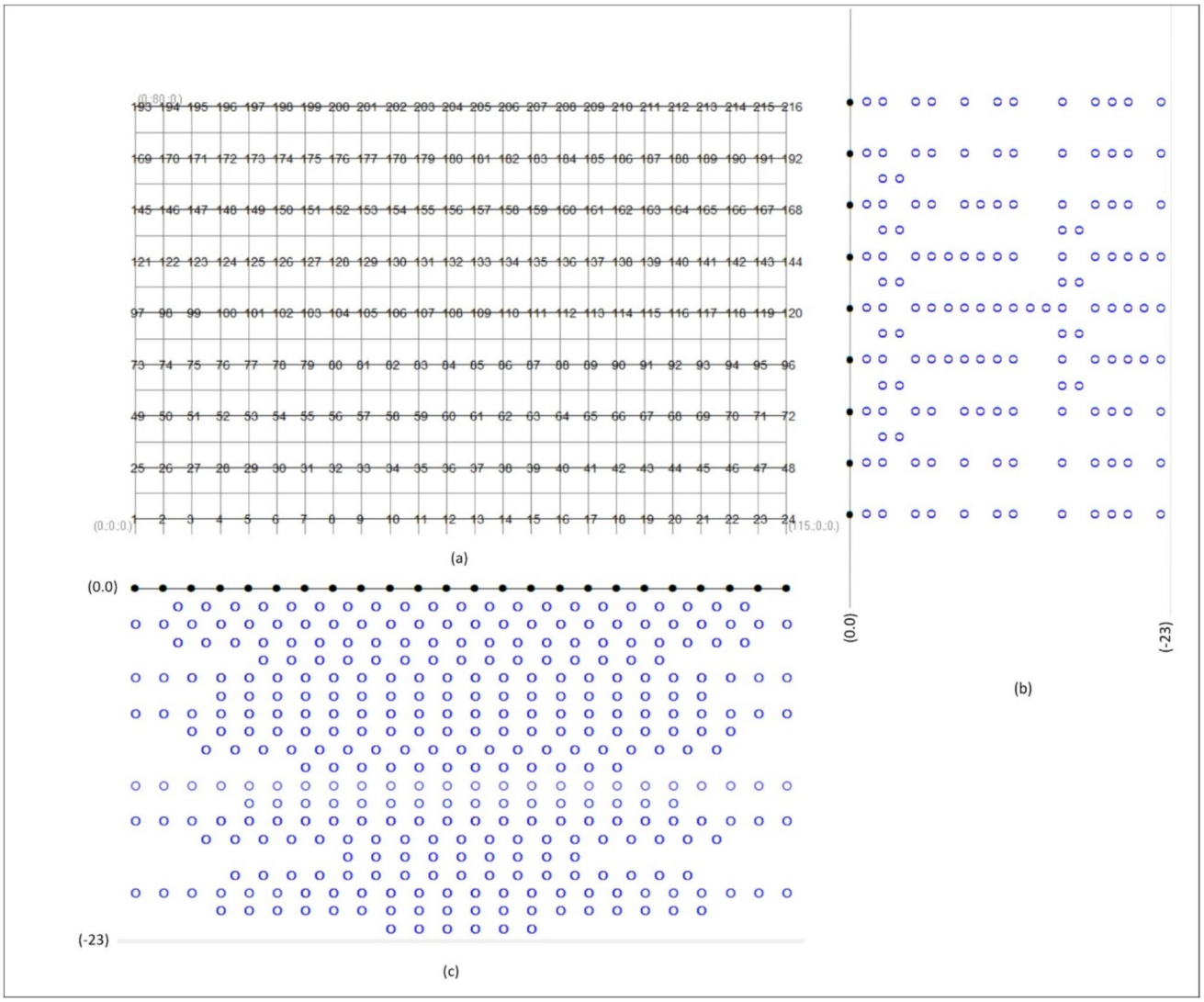

Fig. 8 Electrode configuration for the 3D ERT survey at Solfatara. Geometric arrangement shown in X–Y (**a**), Y–Z (**b**), and X–Z (**c**) planes. Black filled circles represent electrode projections on the X–Z and Y–Z planes; blue open circles represent 3D pseudo-section data points. Electrode IDs are shown in (**a**). This array (9 profiles, 216 electrodes) provided the dense coverage needed for high-resolution 3D inversion

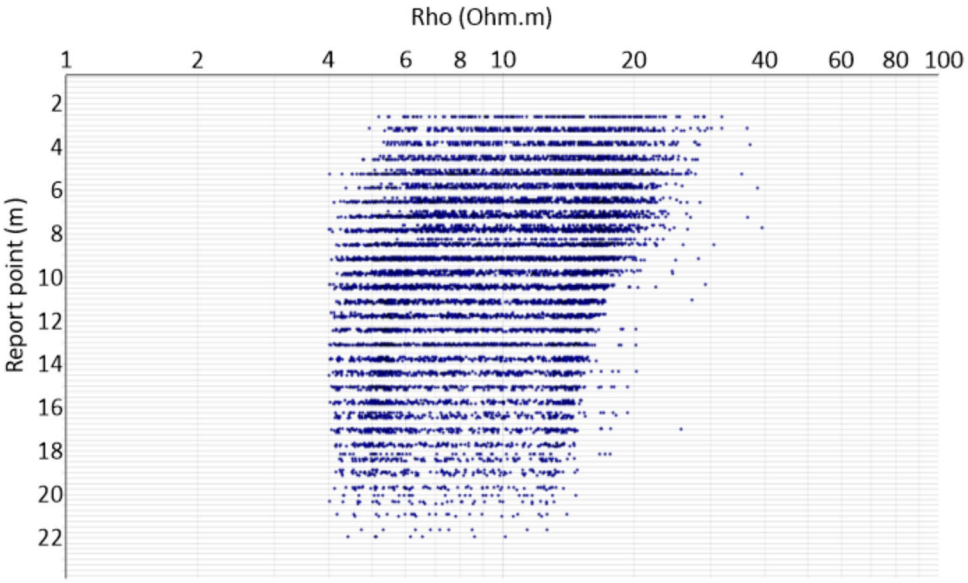

Fig. 9 Apparent resistivity values from the 3D dataset, plotted as a function of pseudo-depth. Spikes and non-physical values were removed during pre-processing. A total of 12,471 quadrupoles were retained for inversion, forming a robust dataset for subsequent finite-element modelling and smoothness-constrained inversion

purely hydrothermal origin unlikely, as volcanic gases such as CO_2, although capable of increasing resistivity, do not generate associated magnetic anomalies. Furthermore, Byrdina et al. (2014) documented that the resistivity interface between liquid water (0.5–5 Ωm) and gas (> 20 Ωm) occurs at ~ 30 m depth in flat areas, significantly deeper than our observed anomaly.

In contrast, lava blocks and related lithologies typically exhibit higher resistivity and coincident magnetic anomalies. Therefore, integrating electrical and magnetic datasets allows us to discard some previous hypotheses and converge toward a more consistent geological interpretation.

Table 1 Parameters of the ERT inversion. RMS vs. iteration number

Iteration No.	RMS (%)
1	18.76
2	12.63
3	9.11
4	8.04
5	6.97
6	5.89
7	4.45
8	2.45
9	2.38
10	2.16
11	2.22
12	2.05
13	2.01

Conclusions

This study presents the first high-resolution magnetic map of the Solfatara crater obtained from magnetic gradient tensor measurements. By analyzing the gradients of the magnetic tensor rather than those of the magnetic vector, we achieved improved spatial resolution in detecting magnetic anomalies. The relevance of this new dataset lies in its ability to refine our understanding of the shallow hydrothermal system and the volcanic structures within Solfatara, an especially critical objective given the crater's central role in the recent unrest affecting the Campi Flegrei region.

In the central sector of Solfatara, the magnetic map reveals dominant NE and NW trends that correspond to the well-established Apennine and anti-Apennine structural orientations. While some of these lineaments coincide with previously mapped faults, others are newly recognized. Importantly, many fault orientations described in earlier field surveys do not display a clear magnetic signature in our dataset.

The total magnetic intensity field also delineates several small-scale anomalies (10–20 m in extent), mainly associated with shallow petrophysical and structural heterogeneities near the crater surface. Interpreting these features, however, requires comparison with complementary geophysical datasets, which enables the development of a more consistent geostructural model in the highly complex setting of Solfatara.

To illustrate this, we compared results from 3D electrical resistivity tomography (ERT) with those derived from magnetic data. Specifically, the TMI vector was reconstructed from the three components of its gradient tensor,

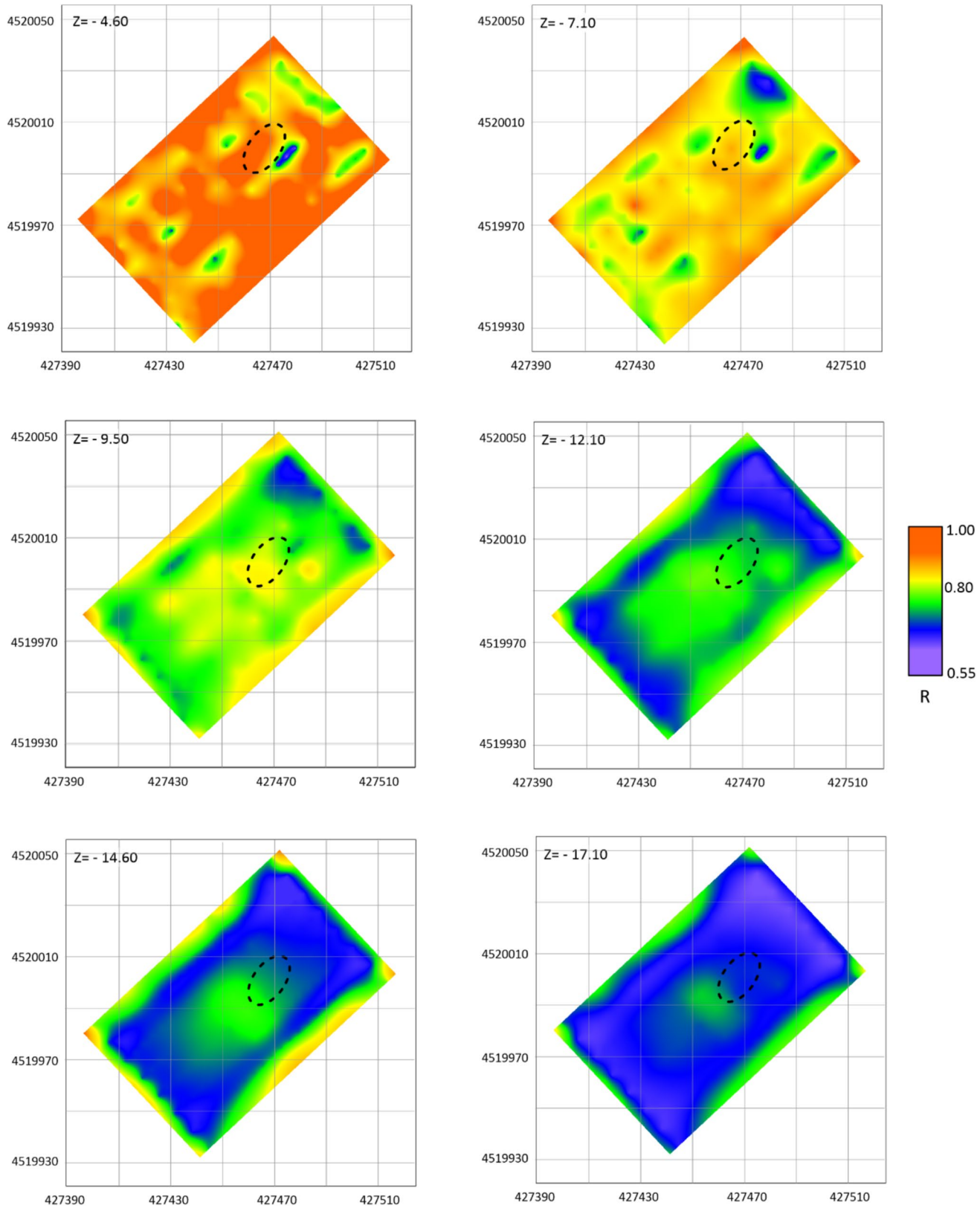

Fig. 10 Resolution model *R* computed for the 3D ERT data using the approach proposed by Day-Lewis et al. (2004). The slices are taken at the same depths as those of the resistivity model obtained from data inversion. At the depths where the resistivity anomaly is observed (7.10–12.10 m), the *R* value is approximately 0.80, indicating good resolution of the resulting model

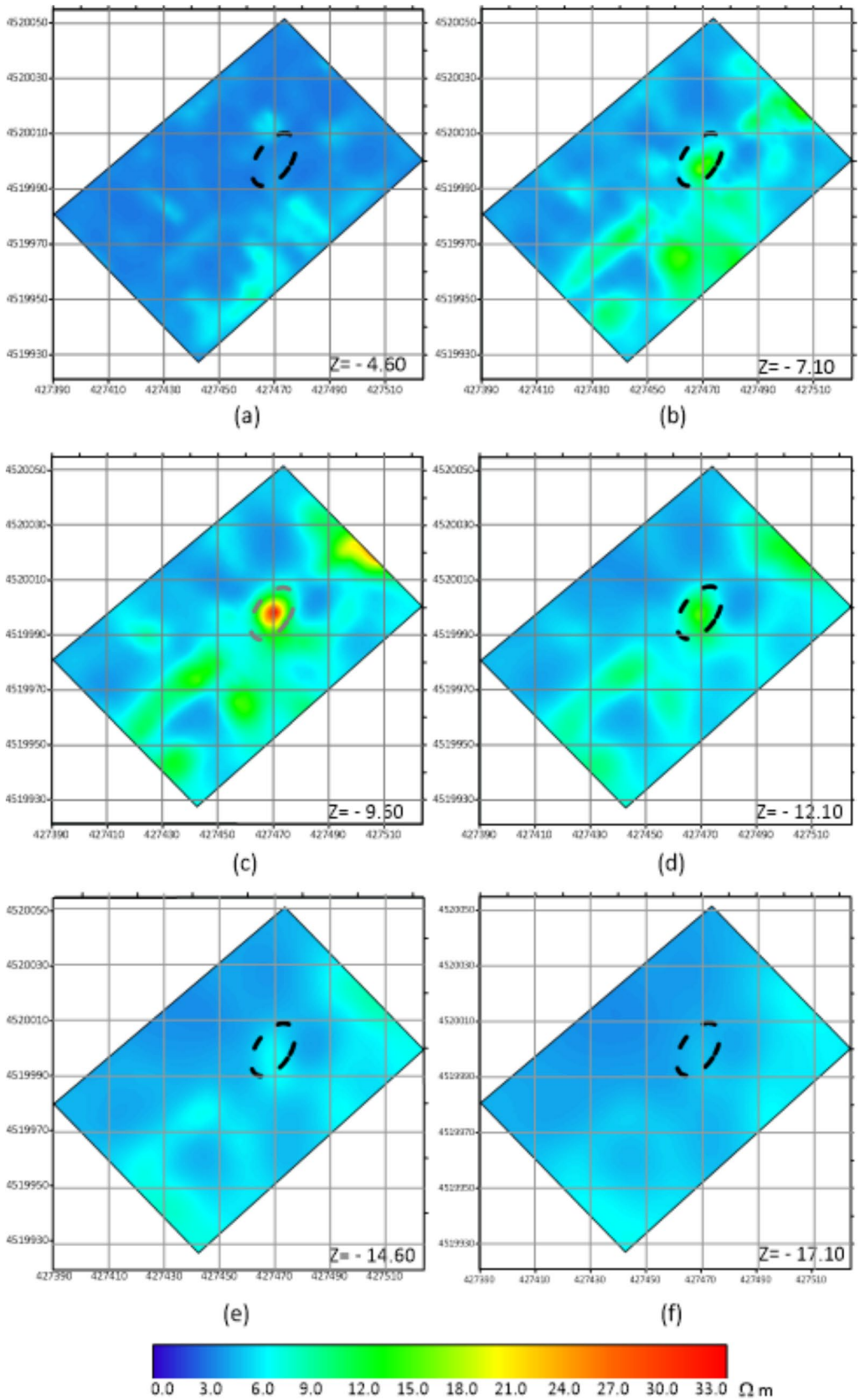
Z= - 4.60
(a)
Z= - 7.10
(b)
Z= - 9.50
(c)
Z= - 12.10
(d)
Z= - 14.60
(e)
Z= - 17.10
(f)
0.0 3.0 6.0 9.0 12.0 15.0 18.0 21.0 24.0 27.0 30.0 33.0 Ω m

◂**Fig. 11** Horizontal resistivity slices from the 3D ERT model, extracted every 2.5 m between depths of 4.60 and 17.10 m below the surface. Resistivity values are generally low (3–35 Ωm), but a distinct NE-elongated anomaly (25–30 Ωm) is evident, outlined by the dashed ellipse. This anomaly is consistently detectable between ~ 7.10 and 14.60 m depth and coincides with features observed in the magnetic data (Figs. 3 and 7)

thereby avoiding orientation errors that often affect direct magnetic vector measurements.

This comparison showed that magnetic gradient tensor displays a stronger spatial correlation with the ERT anomalies. In particular, both the maxima and geometry of the gradient tensor anomaly exhibit a close match with the resistivity anomaly in the ERT slices, providing enhanced precision in locating subsurface features.

Overall, the survey demonstrates that comparing 3D resistivity models with magnetic gradient tensor data significantly improves the detection and characterization of buried volcanic structures. In particular, the joint interpretation supports the recognition of an altered block of the Solfatara cryptodome, alternatively interpretable as a large ballistic lithic block currently exposed in the northeastern sector of the crater.

Appendix

Table 2

Symbol	Name	SI unit
TMI	Total Magnetic Intensity	nT
$\overrightarrow{\text{TMIG}}$	Total Magnetic Intensity gradient	nT/m
MGT	Magnetic Gradient Tensor	nT/m
$\overrightarrow{\text{FVMG}}$	Full Vertical Magnetic Gradient	nT/m
$\overrightarrow{\text{FHMG}}$	Full Horizontal Magnetic Gradient	nT/m
$\vec{B}$	Magnetic induction	nT
ψ	Magnetic potential	A
F	Fourier transform	--

Derivation of the magnetic tensor gradient (**MGT**).

The **MGT** is defined as a vector gradient of the magnetic induction $\vec{B}$ (Beiki et al. 2012).

$$\mathbf{MGT} = \nabla\vec{B} \tag{1}$$

Using Cartesian coordinates (x, y, z) the **MGT** magnetic gradient tensor of $\vec{B}$ in terms of $\nabla\vec{B}$ (Pedersen and Rasmussen 1990):

$$\mathbf{MGT} = \begin{bmatrix} \frac{\partial B_x}{\partial x} & \frac{\partial B_y}{\partial x} & \frac{\partial B_z}{\partial x} \\ \frac{\partial B_x}{\partial y} & \frac{\partial B_y}{\partial y} & \frac{\partial B_z}{\partial y} \\ \frac{\partial B_x}{\partial z} & \frac{\partial B_y}{\partial z} & \frac{\partial B_z}{\partial z} \end{bmatrix} \tag{2}$$

For magnetostatic field, in absence of conduction current, the magnetic induction $\vec{B}$ is irrotational and therefore:

$$\nabla x\vec{B} = 0; \tag{3}$$

If we consider the Earth's magnetic field, it is constituted from multiple sources:

$$\vec{B}_{\text{total}} = \vec{B}_{\text{core}} + \vec{B}_{\text{anomaly}} \tag{4}$$

where $\vec{B}_{\text{core}}$ includes dominant core field while $\vec{B}_{\text{anomaly}}$ includes crustal anomaly field.

The core field contains both spatial and temporal variation while an anomaly field changes only on geological time scales. Anomaly field spatial variation has a small wavelength than the temporal variation of the anomaly field (Getscher and Frontera 2019).

So it is important to note that measuring the gradient of the TMI does not need for subtracting the core field, as is recommended for TMI.

If $\Delta\psi$ is the anomaly in magnetic potential, at all points of free space, it satisfies the Laplace equation

$$\nabla^2(\Delta\psi) = 0 \tag{5}$$

If $\vec{B}_{\text{anomaly}}$ is the anomalous field vector is measured by TMI, we have

$$\vec{B}_{\text{anomaly}} = -\frac{\partial(\Delta\psi)}{\partial\vec{\mathbf{r}}} \tag{6}$$

where $\vec{r}$

is denotes the unit vector in the direction of the earth's field.

The magnetic induction $\vec{B}$ can be expressed as gradient derivatives of the scalar potential ψ (Blakely 1996)

$$\{B_x, B_y, B_z\} = -\nabla\psi; \tag{7}$$

Operating on each side of Eq. (6) with first derivatives and combining them with Eq. (7), we can obtain the following equation:

$$\left\{ \begin{array}{l} \frac{\partial(\vec{B}_{\text{anomaly}})}{\partial x} = \frac{\partial(\vec{B}_x)}{\partial\mathbf{r}} \\ \frac{\partial(\vec{B}_{\text{anomaly}})}{\partial y} = \frac{\partial(\vec{B}_y)}{\partial\mathbf{r}} \\ \frac{\partial(\vec{B}_{\text{anomaly}})}{\partial z} = \frac{\partial(\vec{B}_z)}{\partial\mathbf{r}} \end{array} \right\} \tag{8}$$

Operating on each side of Eq. (8) with 2D Fourier transform and using the time-domain differential theorem of Fourier transform, we obtain

$$\begin{Bmatrix} i\bullet k_x \bullet F\left[\overrightarrow{\mathrm{TMIG}}\right] = i\bullet\alpha\bullet k_x \bullet F\left[B_x\right] + i\bullet\beta\bullet k_y \bullet F\left[B_x\right] + \gamma\bullet k\bullet F\left[B_x\right] \\ i\bullet k_y \bullet F\left[\overrightarrow{\mathrm{TMIG}}\right] = i\bullet\alpha\bullet k_x \bullet F\left[B_y\right] + i\bullet\beta\bullet k_y \bullet F\left[B_y\right] + \gamma\bullet k\bullet F\left[B_y\right] \\ k\bullet F\left[\overrightarrow{\mathrm{TMIG}}\right] = i\bullet\alpha\bullet k_x \bullet F\left[B_z\right] + i\bullet\beta\bullet k_y \bullet F\left[B_z\right] + \gamma\bullet k\bullet F\left[B_z\right] \end{Bmatrix} \tag{9}$$

Equation (9) can be rewritten as the following vertical vector transform operator:

$$\begin{Bmatrix} F\left[B_x\right] = \frac{i\bullet k_x}{i\bullet(\alpha\bullet k_x+\beta\bullet k_y)+\gamma\bullet k}\bullet F\left[\overrightarrow{\mathrm{TMIG}}\right] \\ F\left[B_y\right] = \frac{i\bullet k_y}{i\bullet(\alpha\bullet k_x+\beta\bullet k_y)+\gamma\bullet k}\bullet F\left[\overrightarrow{\mathrm{TMIG}}\right] \\ F\left[B_z\right] = \frac{i\bullet k_z}{i\bullet(\alpha\bullet k_x+\beta\bullet k_y)+\gamma\bullet k}\bullet F\left[\overrightarrow{\mathrm{TMIG}}\right] \end{Bmatrix} \tag{10}$$

where $k = \sqrt{k_x^2 + k_y^2}$, k_xek_y are spatial frequencies in horizontal directions.

Doing the 2D Fourier transform for the Eq. (8), we have:

$$\begin{bmatrix} i\bullet k_x \bullet F\left[B_x\right] & i\bullet k_x\bullet F\left[B_y\right] & i\bullet k_x \bullet F\left[B_z\right] \\ i\bullet k_y \bullet F\left[B_x\right] & i\bullet k_y \bullet F\left[B_y\right] & i\bullet k_y\bullet F\left[B_z\right] \\ k\bullet F\left[B_x\right] & k\bullet F\left[B_y\right] & k\bullet F\left[B_z\right] \end{bmatrix} \tag{11}$$

According to the Eq. (10), we can obtain the relation between the horizontal and vertical component of $\vec{\mathrm{B}}$.

$$\begin{Bmatrix} F\left[B_x\right] = \frac{k_x}{k_y}\bullet F\left[B_y\right] \\ F\left[B_x\right] = i\bullet\frac{k_x}{k}\bullet F\left[B_z\right] \\ F\left[B_y\right] = i\bullet\frac{k_y}{k}\bullet F\left[B_z\right] \end{Bmatrix} \tag{12}$$

By substituting Eq. (12) into Eq. (11), we obtain the relation between vertical magnetic vector and components of **MGT** in Fourier transform (F[**MGT**])

$$\mathrm{F}[\mathbf{MGT}] = \begin{bmatrix} -\frac{k_x^2}{k} & -\frac{k_x\bullet k_y}{k} & -i\bullet k_x \\ -\frac{k_x\bullet k_y}{k} & -\frac{k_y^2}{k} & -i\bullet k_y \\ -i\bullet k_x & -i\bullet k_y & k \end{bmatrix}\bullet F\left[B_z\right]; \tag{13}$$

According to Eqs. (10) and (13), we obtain the calculation of MGT from total magnetic anomaly field in Fourier transform.

$$\mathrm{F}[\mathbf{MGT}] = \begin{bmatrix} \frac{-k_x^2}{i\bullet(\alpha\bullet k_x+\beta\bullet k_y)+\gamma\bullet k} & \frac{-k_x\bullet k_y}{i\bullet(\alpha\bullet k_x+\beta\bullet k_y)+\gamma\bullet k} & \frac{i\bullet k_x\bullet k}{i\bullet(\alpha\bullet k_x+\beta\bullet k_y)+\gamma\bullet k} \\ \frac{-k_x\bullet k_y}{i\bullet(\alpha\bullet k_x+\beta\bullet k_y)+\gamma\bullet k} & \frac{-k_y^2}{i\bullet(\alpha\bullet k_x+\beta\bullet k_y)+\gamma\bullet k} & \frac{i\bullet k_y\bullet k}{i\bullet(\alpha\bullet k_x+\beta\bullet k_y)+\gamma\bullet k} \\ \frac{i\bullet k_x\bullet k}{i\bullet(\alpha\bullet k_x+\beta\bullet k_y)+\gamma\bullet k} & \frac{i\bullet k_y\bullet k}{i\bullet(\alpha\bullet k_x+\beta\bullet k_y)+\gamma\bullet k} & \frac{k^2}{i\bullet(\alpha\bullet k_x+\beta\bullet k_y)+\gamma\bullet k} \end{bmatrix}\bullet F\left[F\left[\overrightarrow{\mathrm{TMIG}}\right]\right] \tag{14}$$

Let us define the quantity:

$$\mathrm{Z}\left(k_x, k_x, k, \alpha, \beta, \gamma\right) = \begin{bmatrix} \frac{-k_x^2}{i\bullet(\alpha\bullet k_x+\beta\bullet k_y)+\gamma\bullet k} & \frac{-k_x\bullet k_y}{i\bullet(\alpha\bullet k_x+\beta\bullet k_y)+\gamma\bullet k} & \frac{i\bullet k_x\bullet k}{i\bullet(\alpha\bullet k_x+\beta\bullet k_y)+\gamma\bullet k} \\ \frac{-k_x\bullet k_y}{i\bullet(\alpha\bullet k_x+\beta\bullet k_y)+\gamma\bullet k} & \frac{-k_y^2}{i\bullet(\alpha\bullet k_x+\beta\bullet k_y)+\gamma\bullet k} & \frac{i\bullet k_y\bullet k}{i\bullet(\alpha\bullet k_x+\beta\bullet k_y)+\gamma\bullet k} \\ \frac{i\bullet k_x\bullet k}{i\bullet(\alpha\bullet k_x+\beta\bullet k_y)+\gamma\bullet k} & \frac{i\bullet k_y\bullet k}{i\bullet(\alpha\bullet k_x+\beta\bullet k_y)+\gamma\bullet k} & \frac{k^2}{i\bullet(\alpha\bullet k_x+\beta\bullet k_y)+\gamma\bullet k} \end{bmatrix} \tag{15}$$

we obtain:

$$\mathrm{F}[\mathbf{MGT}] = \mathrm{Z}\left(k_x, k_x, k, \alpha, \beta, \gamma\right)\bullet F\left[F\left[\overrightarrow{\mathrm{TMIG}}\right]\right]; \tag{16}$$

Using Eq. 16, it is possible to derive the **MGT** from the gradiometric magnetic data acquired in the field. To facilitate the interpretation of magnetic data through the application of the **MGT**, it is possible to find a Cartesian system in which **MGT** will contain three invariant components (Pederson and Rasmussen, 1990; Schmidt and Clark 2006).

$$I_0 = \mathrm{trace}\left(\Delta T_S\right) = \sum\nolimits_{i=1}^{3} \Delta T_{Sii} = 0$$

$$I_1 = \lambda_1\lambda_2 + \lambda_2\lambda_3 + \lambda_3\lambda_1$$

$$I_1 = \lambda_1 \cdot \lambda_2 \cdot \lambda_3$$

where $\lambda_1, \lambda_2, \text{and}\lambda_3$ are the eigenvalues of **MGT.**

It can be shown that the quantity $I_0, I_1,$ and I_3 are unchanged by rotation of the coordinates axes, i.e., they are rotational invariants of the **MGT**.

We also diagonalized the **MGT** and calculated the invariant components by using the eigenvalues (Clark 2012). Invariant components provide information on the geometry of the source.

In fact, $I_0 = 0$ when the field is invariant along a particular direction, i.e., if the causative body is 2-D while $I_0 = 1$ for a monopole source (Pedersen and Rasmussen 1990).

Acknowledgements The authors wish to thank Gaetano Festa for the scientific coordination during field operations of MED-SUV RICEN experiments, and Antimo Angelino, Rodolfo Baculo, Michele Iavarone, Paolo Scotto di Vettimo, and Antimo Guarino for technical support provided during the acquisition phase.

Author contributions VDF planned the experiment; performed the data processing and interpretation, and wrote the paper; PPGB supervised the geophysical surveys during the MED-SUV RICEN experiments, assisted the magnetic data interpretation, and wrote the paper; DT, GC, MP, and NP collected, processed the geophysical data, and contributed to data interpretation. All authors contributed to the preparation and review of the manuscript.

Funding Open access funding provided by Consiglio Nazionale Delle Ricerche (CNR) within the CRUI-CARE Agreement. This work used the datasets acquired under the Med-Suv project. MED-SUV has received funding from the European Union's Seventh Program for research, technological development and demonstration under the grant agreement No. 308665.

Data availability Data will be available from the corresponding author on reasonable request.

Declarations

Conflicts of interest The authors declare no competing interests.

Open Access This article is licensed under a Creative Commons Attribution 4.0 International License, which permits use, sharing, adaptation, distribution and reproduction in any medium or format, as long as you give appropriate credit to the original author(s) and the source, provide a link to the Creative Commons licence, and indicate if changes were made. The images or other third party material in this article are included in the article's Creative Commons licence, unless indicated otherwise in a credit line to the material. If material is not included in the article's Creative Commons licence and your intended use is not permitted by statutory regulation or exceeds the permitted use, you will need to obtain permission directly from the copyright holder. To view a copy of this licence, visit http://creativecommons.org/licenses/by/4.0/.

References

Amoroso O, Festa G, Bruno PP, D L, Auria, De Landro G, Di Fiore V, Gammaldi S, Maraio S, Pilz M, Roux P, Russo G, Serlenga V, Serra M, Woith H, Zollo A (2018) Integrated tomographic methods for seismic imaging and monitoring of volcanic caldera structures and geothermal areas. J Appl Geophys 156:16–30. https://doi.org/10.1016/j.jappgeo.2017.11.012

Arboleda-Zapata M, Guillemoteau J, Tronicke J (2022) A comprehensive workflow to analyze ensembles of globally inverted 2D electrical resistivity models. J Appl Geophys 196:104512. https://doi.org/10.1016/j.jappgeo.2021.104512

Balasco M, Lapenna V, Rizzo E, Telesca L (2022) Deep electrical resistivity tomography for geophysical investigations: the state of the art and future directions. Geosciences 12:438. https://doi.org/10.3390/geosciences12120438

Beiki M, Clark DA, Austin JR, Foss CA (2012) Estimating source location using normalized magnetioc source strength calculated from magnetic tensor data. SEG Edition Geophysics 77(6):123–137

Bernardinetti S, Bruno PPG (2019) The hydrothermal system of solfatara crater (Campi Flegrei, Italy) inferred from machine learning algorithms. Front Earth Sci 7:286. https://doi.org/10.3389/feart.2019.0028

Blakely RJ (1996) Potential theory in gravity and magnetic applications. Cambridge University Press, Cambridge

Briggs IC (1974) Machine contouring using minimum curvature. Geophysics 39(1):39–48

Bruno PPG (2004) Structure and evolution of the Bay of Pozzuoli (Italy) using marine seismic reflection data: implications for collapse of the Campi Flegrei caldera. Bull Volcanol 66:342–355

Bruno PPG, Rapolla A, Di Fiore V (2003) Structural setting of the Bay of Naples (Italy) seismic reflection data: implications for Campanian volcanism. Tectonophysics 372(3–4):193–213

Bruno PPG, Ricciardi GP, Petrillo Z, Di Fiore V, Troiano A, Chiodini G (2007) Geophysical and hydrogeological experiments from a shallow hydrothermal system at Solfatara Volcano, Campi Flegrei, Italy: response to caldera unrest. Journal of Geophysical Research: Solid Earth. https://doi.org/10.1029/2006JB004383

Bruno PPG, Maraio S, Festa G (2017) The shallow structure of Solfatara Volcano, Italy, revealed by dense, wide-aperture seismic profiling. Sci Rep 7:17386. https://doi.org/10.1038/s41598-017-17589-3

Bulent O (2010) Depth estimation of simple causative sources from gravity gradient tensor invariants and vertical component. Pure Appl Geophys 167:1259–1272. https://doi.org/10.1007/s00024-009-0021-4

Byrdina S, Vandemeulebrouck J, Cardellini C, Legaz A, Camerlynckc C, Chiodini G, Lebourg T, Gresse M, Bascou P, Motos G, Carrier A, Caliro S (2014) Relations between electrical resistivity, carbon dioxide flux, and self-potential in the shallow hydrothermal system of Solfatara (Phlegrean Fields, Italy). J Volcanol Geotherm Res 283:172–182

Calò M, Tramelli A (2018) Anatomy of the Campi Flegrei caldera using enhanced seismic tomography models. Sci Rep. https://doi.org/10.1038/s41598-018-34456-x

Calò M, Tramelli A (2025) Evidences of the structures controlling the unrest in Campi Flegrei, Italy; joint interpretation of ambient noise and local earthquake tomography. J Volcanol Geotherm Res. https://doi.org/10.1016/j.jvolgeores.2024.108236

Cardellini C, Chiodini G, Frondini F, Avino R, Bagnato E, Caliro S, Lelli M, Rosiello A (2017) Monitoring diffuse volcanic degassing during volcanic unrests: the case of Campi Flegrei (Italy). Sci Rep 7:6757

Chiodini G, Frondini F, Cardellini C, Granieri D, Marini L, Ventura G (2001) CO2 degassing and energy release at Solfatara volcano, Campi Flegrei, Italy. J Geophys Res 106(B8):16213–16221

Chiodini G, Vilardo G, Augusti V, Granieri D, Caliro S, Minopoli C, Terranova C (2007) Thermal monitoring of hydrothermal activity by permanent infrared automatic stations: results obtained at Solfatara di Pozzuoli, Campi Flegrei (Italy). J Geophys Res 112:B12206. https://doi.org/10.1029/2007JB005140

Chiodini G, Paonita A, Aiuppa A, Costa A, Caliro S, De Martino P, Acocella V, Vandemeulebrouck J (2016) Magmas near the critical

degassing pressure drive volcanic unrest towards a critical state. Nat Commun 7:13712
Chiodini G, Giudicepietro F, Vandemeulebrouck J, Aiuppa A, Caliro S, De Cesare W, Tamburello G, Avino R, Orazi M, D'Auria L (2017) Fumarolic tremor and geochemical signals during a volcanic unrest Available to Purchase. Geology 45:12. https://doi.org/10.1130/G39447.1
Clark DA (2012) New methods for interpretation of magnetic vector and gradient tensor data I: eigenvector analysis and the normalised source strength. Explor Geophys 43(4):267–282
Clark DA (2013) New methods for interpretation of magnetic vector and gradient tensor data II: application to the Mount Leyshon anomaly, Queensland, Australia. Explor Geophys 44(2):114–127
Constable SC, Parker RL, Constable CG (1987) Occam's inversion: a practical algorithm for generating smooth models from electromagnetic sounding data. Geophysics 52:289–300
Cooper GRJ, Cowan DR (2011) A generalized derivative operator for potential field data. Geophys Prospect 59:188–194. https://doi.org/10.1111/j.1365-2478.2010.00901.x
D'Auria L, Giudicepietro F, Aquino I, Borriello C, Del Gaudio D, Lo Bascio M, Martini M, Ricciardi GP, Ricciolino P, Ricco C (2011) Repeated fluid-transfer episodes as a mechanism for the recent dynamics of Campi Flegrei caldera (1989–2010). J Geophys Res Solid Earth 116(B4). https://doi.org/10.1029/2010JB007837
Danesi S, Pino NA, Carlino S, Kilburn C (2023) Relative earthquake location of low-energy volcanic seismicity at Campi Flegrei. Copernicus Meetings (No. EGU23-13351). https://doi.org/10.5194/egusphere-egu23-13351
Day-Lewis FD, Singha K, Binley AM (2004) Applying petrophysical models to radar travel time and electrical resistivity tomograms: resolution-dependent limitations. J Geophys Res 110:B08206
De Martino P, Guardato S, Donnarumma GP, Dolce M, Trombetti T, Chierici F, Macedonio G, Beranzoli L, Iannaccone G (2020) Four years of continuous seafloor displacement measurements in the Campi Flegrei caldera. Front Earth Sci 8:615178. https://doi.org/10.3389/feart.2020.615178
De Martino P, Dolce M, Brandi G, Scarpato G, Tammaro U (2021) The ground deformation history of the Neapolitan Volcanic Area (Campi Flegrei Caldera, Somma-Vesuvius Volcano, and Ischia Island) from 20 years of continuous GPS observations (2000–2019). Remote Sens 13(14):2725. https://doi.org/10.3390/rs13142725
De Siena L, Del Pezzo E, Bianco F (2010) Seismic attenuation imaging of Campi Flegrei: evidence of gas reservoirs, hydrothermal basins, and feeding systems. J Geophys Res Solid Earth. https://doi.org/10.1029/2009JB006938
deGroot-Hedlin C, Constable S (1990) Occam's inversion to generate smooth, two-dimensional models from magnetotelluric data. Geophysics 55:1613–1624. https://doi.org/10.1190/1.1442813
Deino AL, Orsi G, de Vita S, Piochi M (2004) The age of the Neapolitan Yellow Tuff caldera-forming eruption (Campi Flegrei caldera–Italy) assessed by 40Ar/39Ar dating method. J Volcanol Geotherm Res 133:157–170. https://doi.org/10.1016/S0377-0273(03)00396-2
Di Fiore V, Punzo M, Pelosi N, Scotto di Vettimo P, Iavarone M, Budillon F, Zeni G, Lirer F (2019) Electromagnetic field evaluation and EMI on board during a marine geophysical data acquisition (COSMEI). Measurement 147. https://doi.org/10.1016/j.measurement.2019.106889
Di Luccio F, Pino NA, Piscini A, Ventura G (2015) Significance of the 1982–2014 Campi Flegrei seismicity: preexisting structures, hydrothermal processes, and hazard assessment. Geophys Res Lett 42(18):7498–7506
Di Uccio F, Lomax A, Natale J, Muzellec T, Festa G, Nazeri S, Convertito V, Bobbio A, Strumia C, Zollo A (2024) Delineation and fine-scale structure of fault zones activated during the 2014–2024 unrest at the Campi Flegrei caldera (Southern Italy) from high-precision earthquake locations. Geophys Res Lett 51. https://doi.org/10.1029/2023GL107680
Esposito AM, De Cesare W, Macedonio G, Giudicepietro F (2023) Efficient SOM's application to seismic fumarolic tremor for the detection of anomalous hydrothermal activity in Campi Flegrei volcano (Italy). Appl Sci 13(9):5505
Finetti I, Morelli C (1974) Esplorazione sismica a riflessione dei golfi di Napoli e Pozzuoli . Boll Geof Teor e Appl Trieste 16 (62–63), 175–222
Fitzgerald D, Argas TD, Paterson R, Holstein H (2010) Full tensor magnetic gradiometry processing and interpretation developments. 11th SAGA Biennial Technical Meeting and Exhibition, Sep 2009, cp-241-00056. https://doi.org/10.3997/2214-4609-pdb.241.fitzgerald_paper3
Florio G, Fedi M, Cella F, Rapolla A (1999) The Campanian Plain and Phlegrean Fields: structural setting from potential field data. J Volcanol Geotherm Res 91:361–379
Getscher T, Frontera P (2019) Magnetic gradient tensor framework for attitude-free position estimation, proceedings of the 2019 International Technical Meeting of The Institute of Navigation, Reston, Virginia, January 2019, pp 495–507. https://doi.org/10.33012/2019.16706
Giaccio B, Hajdas I, Isaia R, Deino A, Noma S (2017) High-precision 14C and 40Ar/39Ar dating of the Campanian Ignimbrite (Y-5) reconciles the time-scales of climatic-cultural processes at 40 ka. Scientific Reports 7. https://doi.org/10.1038/srep45940
Giudicepietro F, Ricciolino P, Bianco F, Caliro, S, Cubellis E, D'Auria L, De Cesare W, De Martino, P, Esposito A, Galluzzo D, Macedonio G, Lo Bascio ., Orazi M, Pappalardo L, Peluso R, Scarpato G, Tramelli A, Chiodini G (2021). Campi Flegrei, Vesuvius and Ischia seismicity in the context of the Neapolitan Volcanic area. **, 9. https://doi.org/10.3389/feart.2021.662113.
Gresse M, Vandemeulebrouck J, Byrdina S, Chiodini G, Revil A, Johnson TC, Metral L (2017) Three-dimensional electrical resistivity tomography of the Solfatara crater (Italy): implication for the multiphase flow structure of the shallow hydrothermal system. J Geophys Res Solid Earth 122:8749–8768
Hardwick CD (1996) Aeromagnetic gradiometry in 1995. Explor Geophys 27:1–11
Hardwick CD (1999) Gradient-enhanced total field gridding. Expanded Abstracts in SEG Houston, Gravity and Magnetics 2:7
Harrison C, Southam JR (1991) Magnetic field gradients and their uses in the study of the earth's magnetic field. J Geomagn Geoelectr 43:7. https://doi.org/10.5636/jgg.43.585
Hood P (1981) Aeromagnetic gradiometry: a superior geological mapping tool for mineral exploration programs, In: (Ed. H. Weinstock and W.C. Overton) SQUID Applications to Geophysics, Proceedings of the Workshop held 2-4 June 1980, Los Alamos, Soc Expl Geophys, Tulsa, Oklahoma, 72-76
Hood P, McClure DJ (1965) Gradient measurements in ground magnetic prospecting. Geophysics 30:403–410
Hood PJ, Teskey DJ (1989) Aeromagnetic gradiometer program of the Geological Survey of Canada. Geophysics 54(8):1012–1022
Isaia R, Marianelli P, Sbrana A (2009) Caldera unrest prior to intense volcanism in Campi Flegrei (Italy) at 4.0 ka B.P.: implications for caldera dynamics and future eruptive scenarios. Geophys Res Lett. https://doi.org/10.1029/2009GL040513
Isaia R, Vitale S, Di Giuseppe MG, Iannuzzi E, Tramparulo F, Troiano A (2015) Stratigraphy, structure and volcano-tectonic evolution of Solfatara maar-diatreme (Campi Flegrei, Italy). GSA Bull 127(9/10):1485–1504. https://doi.org/10.1130/B31183.1
Judenherc S, Zollo A (2004) The Bay of Naples (southern Italy): constraints on the volcanic structures inferred from a dense seismic survey. J Geophys Res Solid Earth. https://doi.org/10.1029/2003JB002876

LaBrecque DJ, Ramirez AL, Daily WD, Binley AM, Schima SA (1996) ERT monitoring of environmental remediation processes. Meas Sci Technol 7:375–383. https://doi.org/10.1088/0957-0233/7/3/019

LaBrecque DJ, Morelli G, Daily W, Ramirez A, Lundegard P (1999) Occam's inversion of 3-D electrical resistivity tomography. In 'Three-dimensional electromagnetics', Michael Oristaglio and Brian Spies Editor, Publisher: Society of Exploration Geophysicists. https://doi.org/10.1190/1.9781560802154.ch37

Luo Y, Mei-Ping W, Ping W, Shu-Ling D, Hao-Jun L, Jin-Long W, Zhan-Feng A (2015) Full magnetic gradient tensor from triaxial aeromagnetic gradient measurements: calculation and application. Appl Geophys 12(3):283–291. https://doi.org/10.1007/s11770-015-0508-y

Neukirch M, Rudolf D, Garcia X, Galiana S (2019) Amplitude-phase decomposition of the magnetotelluric impedance tensor. Geophysics. https://doi.org/10.1190/geo2018-0352.1

Orsi G, Civetta L, Del Gaudio C, De Vita S, Di Vito MA, Isaia R, Petrazzuoli SM, Ricciardi GP, Ricco C (1999) Short-term ground deformations and seismicity in the resurgent Campi Flegrei caldera (Italy): an example of active block-resurgence in a densely populated area. J Volcanol Geotherm Res 91(2–4):415–451

Pedersen LB, Rasmussen TM (1990) The gradient tensor of potential field anomalies: some implications on data collection and data processing of maps. Geophysics 55:1558–1566

Schmidt PW, Clark DA (2006) The magnetic gradient tensor: its properties and uses in source characterization. Lead Edge 25:75–78

Siniscalchi A, Tripaldi S, Romano G, Chiodini G, Improta L, Petrillo Z, D L, Auria, Caliro S, Avino R (2019) Reservoir structure and hydraulic properties of the Campi Flegrei geothermal system inferred by audiomagnetotelluric, geochemical, and seismicity study. J Geophys Res Solid Earth 124:5336–5356. https://doi.org/10.1029/2018JB016514

Smith VC, Isaia R, Pearce NJG (2011) Tephrostratigraphy and glass compositions of post-15 kyr Campi Flegrei eruptions: implications for eruption history and chronostratigraphic markers. Quat Sci Rev 30:3638–3660. https://doi.org/10.1016/j.quascirev.2011.07.01

Tramelli A, Godano C, Ricciolino P, Giudicepietro F, Caliro S, Orazi M, Martino P, Chiodini G (2021). Statistics of seismicity to investigate the Campi Flegrei caldera unrest. Sci Rep 11. https://doi.org/10.1038/s41598-021-86506-6

Tramelli A, Giudicepietro F, Ricciolino P, Chiodini G (2022) The seismicity of Campi Flegrei in the contest of an evolving long term unrest. Sci Rep. https://doi.org/10.1038/s41598-022-06928-8

Tramelli A, Giudicepietro F, Godano C, Ricciolino P, Orazi M, Caliro S, De Martino P, Chiodini G (2023). The seismicity of Campi Flegrei in the contest of the current unrest Copernicus Meetings (No. EGU23-12800). https://doi.org/10.5194/egusphere-egu23-12800

Troiano A, Isaia R, Di Giuseppe MG, Tramparulo FDA, Vitale S (2019) Deep electrical resistivity tomography for a 3d picture of the most active sector of Campi Flegrei caldera. Sci Rep 9:15124. https://doi.org/10.1038/s41598-019-51568-0

Vanorio T, Virieux J, Capuano P, Russo G (2005) Three-dimensional seismic tomography from P wave and S wave microearthquake travel times and rock physics characterization of the Campi Flegrei Caldera. J Geophys Res 110:B03201. https://doi.org/10.1029/2004JB003102

Zollo A, Maercklin N, Vassallo M, Dello Iacono D, Virieux J, Gasparini P (2008) Seismic reflections reveal a massive melt layer feeding Campi Flegrei caldera. Geophys Res Lett. https://doi.org/10.1029/2008GL034242

Zuo B, Wang L, Chen W (2017) Full tensor eigenvector analysis on airborne magnetic gradiometer data for the detection of dipole-like magnetic source. Sensors 17(9):1976. https://doi.org/10.3390/s17091976